Nano Research

Open Access

Research Article

Controllable assembly of porphyrin/perylene imide for near-infrared photothermal antibacteria

Yisheng Liu[1,2,§], Yingying Shi[1,§], Luman You[1,§], Jianlei Qian[1], Chu Hao[1], Yong Zhong[1], Jiayin Wang[1], Feng Bai[1,3] ✉, and Xiaoyan Yang[1] ✉

[1] *Key Laboratory for Special Functional Materials of Ministry of Education, National and Local Joint Engineering Research Center for High-Efficiency Display and Lighting Technology, School of Nanoscience and Materials Engineering, and Collaborative Innovation Center of Nano Functional Materials and Applications, Henan University, Kaifeng 475004, China*
[2] *International Joint Centre for Biomedical Innovation, School of Life Sciences, Henan University, Kaifeng 475004, China*
[3] *Academy for Advanced Interdisciplinary Studies, Henan University, Kaifeng 475004, China*
§ *Yisheng Liu, Yingying Shi, and Luman You contributed equally to this work.*

Cite this article: *Nano Research*, **2025**, *18*, 94907835. https://doi.org/10.26599/NR.2025.94907835

ABSTRACT: Porphyrins suffer from visible light excitation, which seriously restricts photothermal therapy (PTT) to superficial lesions. Developing porphyrin derivatives with near-infrared (NIR) absorption via chemical synthesis requires complicated synthesis and purification. In this work, the electron acceptor N,N'-di(L-alanine) perylene diimide (PDI) was introduced to the electron donor tetraminophenyl porphyrin (TAPP) to prepare the charge-transfer TAPP/PDI nanoparticles (NPs) as an NIR activatable photothermal agent via a simple and efficient nanoprecipitation method. When the molar ratio of TAPP to PDI was 1:2, uniformly dispersed TAPP/PDI NPs were obtained with a new NIR absorption peak (758 nm), along with fluorescence emission quenching. These results indicated that the charge transfer from the donor to the acceptor occurred within the TAPP/PDI NPs. The co-assembly forces were proven to originate from π−π interactions and hydrogen bond interactions, according to experiment results and molecular dynamic simulation. Furthermore, the energy gap of TAPP/PDI dimer was significantly narrowed, however, the spin-orbit coupling (SOC) constant was too small for intersystem crossing, which in favor of the NIR light activated non-radiative transition of TAPP/PDI NPs. Consistent with theoretical calculations, TAPP/PDI NPs could effectively generate heat with photothermal conversion efficiency (PCE) of 36.5% under the illumination of 808 nm laser. Antibacterial experiments demonstrated that TAPP/PDI NPs could induce the death of both Gram-positive *S. aureus* bacteria and Gram-negative *E. coli* bacteria, and could eradicate *S. aureus* infection in mice after only one treatment. Therefore, supramolecular co-assembly affords a facile approach for fabricating NIR activated porphyrin-based photothermal agents (PTAs) for photothermal therapy and beyond.

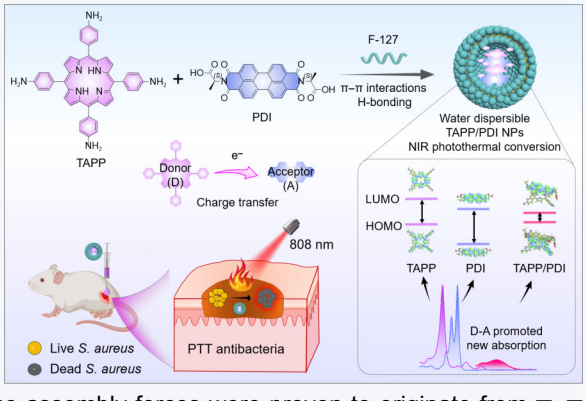

KEYWORDS: tetraminophenyl porphyrin, N,N'-di(L-alanine) perylene diimide, near-infrared, photothermal therapy

1 Introduction

Supramolecular assembly utilizing optically active molecules as building blocks offers an effective approach for constructing nanoscale photothermal agents (PTAs) for photothermal therapy (PTT). PTT [1, 2] uses PTAs to transfer light energy into heat, thereby killing bacteria. This modality has emerged as a pivotal approach for effectively combating bacterial infections, featuring high selectivity, non-invasiveness, broad-spectrum antibacterial properties, less drug resistance, and low toxicity [3–5]. Porphyrins possess rigid π-conjugated structures, good biogenicity, and excellent light energy conversion properties, positioning them suitable for molecular assembly [6–8]. Leveraging supramolecular interactions, self-assembled porphyrins may demonstrate enhanced photophysical properties, combined with improved nonradiative decay (internal conversion) or increased reactive oxygen species (ROS) production [9–11]. However, their dependence on visible

Received: May 19, 2025; **Revised:** July 20, 2025
Accepted: July 23, 2025

✉Address correspondence to Feng Bai, baifengsun@126.com; Xiaoyan Yang, xiaoyanyang@henu.edu.cn

light excitation restricts therapeutic applications to superficial lesions [12]. Therefore, developing porphyrin-based near-infrared (NIR, 750–1700 nm) PTAs is essential to improve the photothermal antibacterial efficacy.

Researchers have synthesized a series of porphyrins derivatives with NIR absorption via chemical synthesis. For example, to extend the π-conjugation length, Narita et al. fused porphyrins with one or two nanographene units to fabricate nanographene-porphyrin hybrids (NGP-1 and NGP-2), which exhibited absorption extending to ≈ 1000 and ≈ 1400 nm, respectively [13]. Zeng et al. synthesized an A-D-A structured porphyrin (PPor) derivate by conjugating porphyrin to perylene diimide (PDI), which could self-assemble into nanoparticles (NPs) with NIR absorbance peak at 860 nm, attributed to the internal charge transfer (CT) effect [14]. Wong synthesized two porphyrin derivates ZnP-CPDT and ZnP-BT with A-π-D-π-A structure, which showed absorption ranging from 370 to 800 nm in free molecular form [15]. However, the molecular engineering strategy involves complicated synthesis and extremely troublesome purification, while the supramolecular assembly method would be more convenient and efficient. The charge-transfer assemblies (CTA) could achieve spectral regulation, which might be superior than the constituent components, due to the CT from electron donor to acceptor [16, 17]. For example, tetraminophenyl porphyrin (TAPP) could form ordered J-aggregates (TAPP-O NPs), which show obvious bathochromic shift to ~ 710 nm [18, 19]. When 7,7,8,8-tetracyanoquinodimethane (TCNQ, the electron acceptor) was introduced to TAPP, the obtained charge-transfer TAPP-TCNQ NPs showed an NIR absorption peak and photothermal conversion efficiency (PCE) of 23.1% [20]. To enhance the photothermal property of porphyrin near-infrared PTAs, other charge-transfer materials need to be explored.

With a π-conjugated structure, perylene diimides exhibit a large extinction coefficient, high biocompatibility, and strong electron-accepting ability, making them promising candidates for co-assembly with porphyrin [21–25]. However, based on our previous work on porphyrin assembly [26–29], it might be difficult to prepare the co-assemblies only by the π–π interaction, other non-valent interactions such as hydrogen bond interaction need to be introduced. Interestingly, this idea has also been verified by Xie et al. They fabricated TAPP/PDI-G NPs by co-assembly of TAPP and perylene diimide with 4 carboxyl groups (PDI-G), which demonstrated absorption redshift and photothermal effect irradiated by 808 nm laser [30]. However, it is essential to systematically investigate the co-assembly of TAPP and perylene diimide with two carboxyl, because the intermolecular/intramolecular interaction forces-dominated co-assembly process is complicated. More importantly, it is necessary to elucidate the origin of the absorption red-shift and the energy dissipation process, due to their fundamental significance.

In this work, we constructed D-A structured TAPP/PDI NPs for NIR photothermal antibacterial therapy, using TAPP as the electron donor and N,N'-di(L-alanine) PDI as the electron acceptor through a facile nanoprecipitation method. Due to charge transfer, TAPP/PDI NPs showed a new characteristic absorption peak at 758 nm, and fluorescence quenching compared with TAPP NPs. Importantly, theoretical calculation was conducted to comprehensively elucidate the co-assembling forces, the original cause of absorption redshift, and the possible energy dissipation courses. Consistent with theoretical calculations, TAPP/PDI NPs could effectively generate heat with PCE of 36.5% and kill bacteria under the illumination of 808 nm laser. This work represents an important supplementary to the field of near-infrared porphyrin nanomaterials.

2 Experimental

2.1 Materials

TAPP and N,N'-dimethylformamide (DMF) were purchased from Aladdin Chemical Reagent Co., Ltd. PDI was purchased from Bidepharm Chemical Co. Pluronic F-127 was purchased from Sigma Aldrich. Cytotoxicity assay kits (CCK-8) and 2,7-dichlorodihydrofluorescein diacetate (DCFH-DA) were obtained from Beyotime Biotechnology. Ultrapure water (18.2 MΩ·cm) was utilized to prepare aqueous solutions.

2.2 Characterization

The morphological characteristics of the nanomaterials were examined using scanning electron microscopy (SEM, JSM-7900F) and transmission electron microscopy (TEM, JEM-2100). Particle size distribution measurements were performed using dynamic light scattering (DLS, Nano ZS, Malvern). The absorption and fluorescence spectra were measured by ultraviolet–visible (UV–vis) (Agilent Cary60) and fluorescent spectrophotometer (JY HORIBA FluoroLog-3), respectively. Functional group was analyzed through Fourier transform infrared (FT-IR) spectroscopy (Bruker VERTEX70), while crystalline data was obtained on X-ray diffraction (XRD, Bruker D8 Advance). Photothermal experiments employed an 808 nm laser (Haite Optoelectronics Co., Ltd.). Cellular viability assessments were quantified using microplate reader (Tecan, Infinite MPlex). Live/dead cell staining images were acquired using confocal laser scanning microscopy (CLSM, OLYMPUS FV1000). The changes in tumor temperature were recorded using an infrared thermal imaging camera (FlukTIX580, Fluke Company).

2.3 Synthesis of TAPP/PDI NPs

To obtain TAPP/PDI NPs (TAPP to PDI feed ratio of 1:2), 100 μL TAPP in DMF (14.8 mM), and 495 μL PDI in DMF (6 mM) were quickly mixed, and injected into 10 mL F-127 aqueous (1 mg·mL^{-1}), followed by probe sonication (100 W, 3 min). After continuously stirring for 48 h at room temperature, the assemblies were collected by centrifugation (30,000 rpm, 30 min) and rinsed with deionized water for once to remove the excess surfactants. TAPP/PDI NPs were dispersed in ultrapure water.

For the preparation of TAPP/PDI co-assemblies with feed ratio of 1:1, 1:4, and 1:6, the protocol was essentially the same as the procedure used for the preparation of TAPP/PDI NPs (1:2 feed ratio), except that the volume of PDI was changed to 248, 991, and 1490 μL.

For the preparation of TAPP NPs or PDI NWs, the protocol was the same as the procedure used for the preparation of TAPP/PDI NPs (1:2 feed ratio), except for the absence of PDI or TAPP. The TAPP NPs and PDI NWs were collected by centrifugation at speed of 12,000 and 60,000 rpm, respectively for 30 min.

2.4 Photothermal properties of TAPP/PDI NPs

TAPP/PDI NPs (1 mL) were added into the quartz cuvette, and the temperature was monitored by a thermocouple with accuracy of ±

0.1 °C under 808 nm laser irradiation.

The photothermal conversion efficiency (η) under 808 nm laser was calculated through the following formula

$$\eta = \frac{hS\Delta T_{max} - Q_S}{I(1-10^{-A_{808}})} \quad (1)$$

$$hS = \frac{mc}{\tau_S} \quad (2)$$

where m (~ 1.0 g) and c (4.2 J·g^{-1}·°C^{-1}) are the mass and heat capacity of water. hS are calculated according to Eq. (1). τ_s is the time constant and simulated to be 439.2 s. ΔT_{max} equals to T_{max} minus T_{sur}. Q_S is the heat dissipated from quartz cell and water irradiated by laser. Q_S was measured to be 44.8 mW. A_{808} is the absorbance at 808 nm, and I is the laser power density. According to Eq. (2), $\eta_{TAPP/PDI\ NPs}$ = 36.5%.

2.5 Detection of reactive oxygen species

To assess the $^1O_2$ production properties of the assemblies, anthracene-9,10-dipropionic acid (ADPA) (10^{-3} M) was used as an $^1O_2$ indicator and added to each assembly. The samples were irradiated by 808 nm laser (1.0 W·cm^{-2}), and the absorbance was measured at 0, 1, 3, 5, 7, 10 min by a UV–vis spectrophotometer.

The $^1O_2$ generation of TAPP/PDI NPs was further assessed via electron spin resonance (ESR) spectroscopy using TEMP as the spin-trapping reagent, which produced the characteristic 1:1:1 triplet signal. Deionized water served as the control. The ESR spectra were recorded using a computer-coupled spectrometer.

DCFH-DA was utilized as ROS indicator after activated by NaOH. First, 10 μL DCFH-DA (10 mM) was added into 90 μL of NaOH (50 mM) aqueous solution. The solution was sonicated for 30 min under dark at room temperature to cleave the ester bond and generate 2',7'-dichlorodihydrofluorescein (DCFH). After that, 20 μL of DCFH solution was added into TAPP/PDI NPs. The solution was irradiated by 808 nm laser (1.0 W·cm^{-2}), and then the fluorescence spectra were measured at 0, 1, 3, 5 min, with an excitation wavelength of 488 nm.

2.6 Theory calculations

Molecular optimization was conducted firstly at the B3LYP/6-31+G (d, p) level with density functional theory (DFT) using the Gaussian 16 program package. For molecular dynamics simulation, we used the Gromacs software to construct a box of size 3 nm × 3 nm × 3 nm and randomly inserted 5 TAPP molecules and 5 PDI molecules into it. During the simulation process, we first carried out 2 ns of NVT and 5 ns of NPT ensemble to pre-equilibrate the system, and then conducted a 1 ns molecular dynamics simulation to obtain information on the intermolecular interactions.

Then the absorption-related information was obtained with DFT using Gaussion. Excited-state properties were evaluated via time-dependent density functional theory (TD-DFT) with the PBE/6-31G** method for both monomeric and dimeric systems, incorporating five singlet and five triplet excited states. Subsequent optimizations of the singlet and triplet excited states were carried out at the same level of theory using the unrestricted formalism. Molecular orbital visualization was achieved using VMD, GaussView, and Multiwfn [31–33].

2.7 Bacterial culture

Bacterial strains (*S. aureus* or *E. coli*) were incubated at 37 °C overnight in Luria-Bertani (LB) broth under shaking conditions. Afterwards, the bacteria were collected by centrifugation (3000 rpm, 5 min), rinsed thrice with saline, and re-dispersed in saline for later experiment.

2.8 *In vitro* antibacterial assay

Firstly, the antibacterial efficacy of TAPP/PDI NPs was evaluated using the standard spread plate method. Bacterial suspensions were treated with varying concentrations of TAPP/PDI NPs (determined by the amount of TAPP), and then irradiated with 808 nm laser (1.0 W·cm^{-2}, 10 min) or kept in dark conditions as control. Subsequently, the bacterial suspension was washed with saline, then serially diluted and 100 μL solution was plated on LB. Following 24 h incubation, bacterial viability was determined by colony enumeration and photographic documentation of the plates.

Following different treatments, the bacterial cells were collected by centrifugation (3000 rpm, 5 min) and fixed with 2.5% glutaraldehyde at 4 °C overnight. Subsequently, the samples were dehydrated for 5 min through a graded ethanol series (30%, 50%, 70%, 90%, and 100%) before SEM characterization.

Additionally, bacterial suspension was stained with SYTO9/PI dyes (3 μL, 1:1, v/v) for 15 min under dark after different treatment, then observed via a CLSM.

2.9 *In vitro* cell cytotoxicity assay of TAPP/PDI NPs

The cytotoxicity of TAPP/PDI NPs was assessed by CCK-8 assay using HeLa cells. After incubated in the 96-well plates overnight at 37 °C containing 5% CO_2, the Hela cells were cultured with Dulbecco's modified eagle medium (DMEM) (100 μL) containing TAPP/PDI NPs (TAPP concentration of 0, 100, 200, 300, and 400 μg·mL^{-1}) for 8 h. After discarding the culture medium, cells were treated with CCK-8 solution (100 μL, diluted 1:10 in medium). Microplate reader was utilized to record the absorbance at 450 nm.

2.10 Hemolysis assay

Whole blood from mice was centrifuged (3000 rpm, 5 min) to separate the red blood cells (RBCs) from serum and washed three times with PBS. The RBCs were then resuspended to prepare 50% (v/v) suspensions in deionized water (positive control), PBS (negative control), and TAPP/PDI NPs (25, 50, 100, 200, 300, and 400 μg·mL^{-1}). Following a 2-hour incubation at 37 °C, the samples were centrifuged (15,000 rpm, 20 min) to pellet intact erythrocytes. Supernatants (100 μL) were transferred to a 96-well microplates for absorbance measurements at 541 nm using a microplate reader. Concurrently, the erythrocyte pellets were resuspended in PBS (100 μL) for cellular morphology examination by inverted fluorescence microscopy. The equation for calculating hemolysis percentage: Hemolysis (%) = (A_{sample} − $A_{negative\ control}$)/($A_{positive\ control}$ − $A_{negative\ control}$) × 100%.

2.11 *In vivo* wound healing assay

Female ICR mice (5–6 weeks) were procured from SPF (Beijing) Biotechnology Co., Ltd. All experiments were conducted in accordance with the ethical guidelines approved by the Medical and Scientific Research Ethics Committee of Henan University School of Medicine.

To establish mice wound infection model, circular full-thickness cortical wounds with an approximately 8 mm diameter were created, followed by inoculation of *S. aureus* suspension. One day later (day 0), the mice with *S. aureus*-infected wounds were

randomly divided into four groups (n = 6): control, NIR, TAPP/PDI NPs, and TAPP/PDI NPs + NIR. For laser-treated groups, wound was irradiated with 808 nm laser (1.0 W·cm^{-2}, 10 min). Real-time thermal imaging was performed using an infrared camera to monitor temperature variations at the wound site. Wound images were captured using a camera and the mice weights were measured on days 0, 2, 4, 6, 8, and 10, respectively.

To ascertain bacterial burden of each group, the surrounding skin tissue near the wound in each group was harvested and homogenized on day 10. Subsequently, the homogenate was diluted using saline and streaked onto LB plates for colony enumeration, enabling a comprehensive analysis of bacterial colony counts for comparison.

2.12 Tissue sectioning and staining

To assess the degree of wound healing, the infected skins were collected on day 10 for hematoxylin and eosin (H&E) or Masson staining. For further pathological examination, the major organs including heart, liver, spleen, lung, and kidney were obtained for H&E staining (Service bio, Zhengzhou, China).

2.13 Blood routine and biochemistry analysis

The blood samples were collected on day 10 for blood routine examination and inflammatory factor detection to evaluate the level of inflammatory reaction after different treatments (Service bio, Zhengzhou, China).

3 Results and discussion

The synthetic route of TAPP/PDI NPs via nanoprecipitation process is illustrated in Scheme 1. The synthesis was conducted by employing F-127 as the surfactant. As shown in Fig. S1 in the Electronic Supplementary Material (ESM), uniform nanoparticles could be prepared by changing the F-127 concentration from 0.6 to 2.5 mg·mL^{-1}. Strikingly, the nanoparticles showed Q-band absorption red-shifted to 758 nm compared with TAPP monomer and PDI monomer, implying the successfully co-assembly of TAPP and PDI (Fig. S2 in the ESM) [20]. Considering that the assemblies dispersion prepared in the presence of F-127 was very stable without precipitation, we selected 1 mg·mL^{-1} F-127 to study the impact of feed ratio on the assembly behavior. As shown in Fig. S3 in the ESM, uniform nanoparticular morphology could be obtained when the feed molar ratios of TAPP to PDI are 1:1 and 1:2, then mixed morphology arise when the feed molar ratios change to 1:4 and 1:6. Careful studies on the absorption spectra (Fig. S4 in the ESM) showed that a weak NIR peak arose with 1:1 feed ratio, and the NIR peak intensified with 1:2 feed ratio, maintained until 1:4

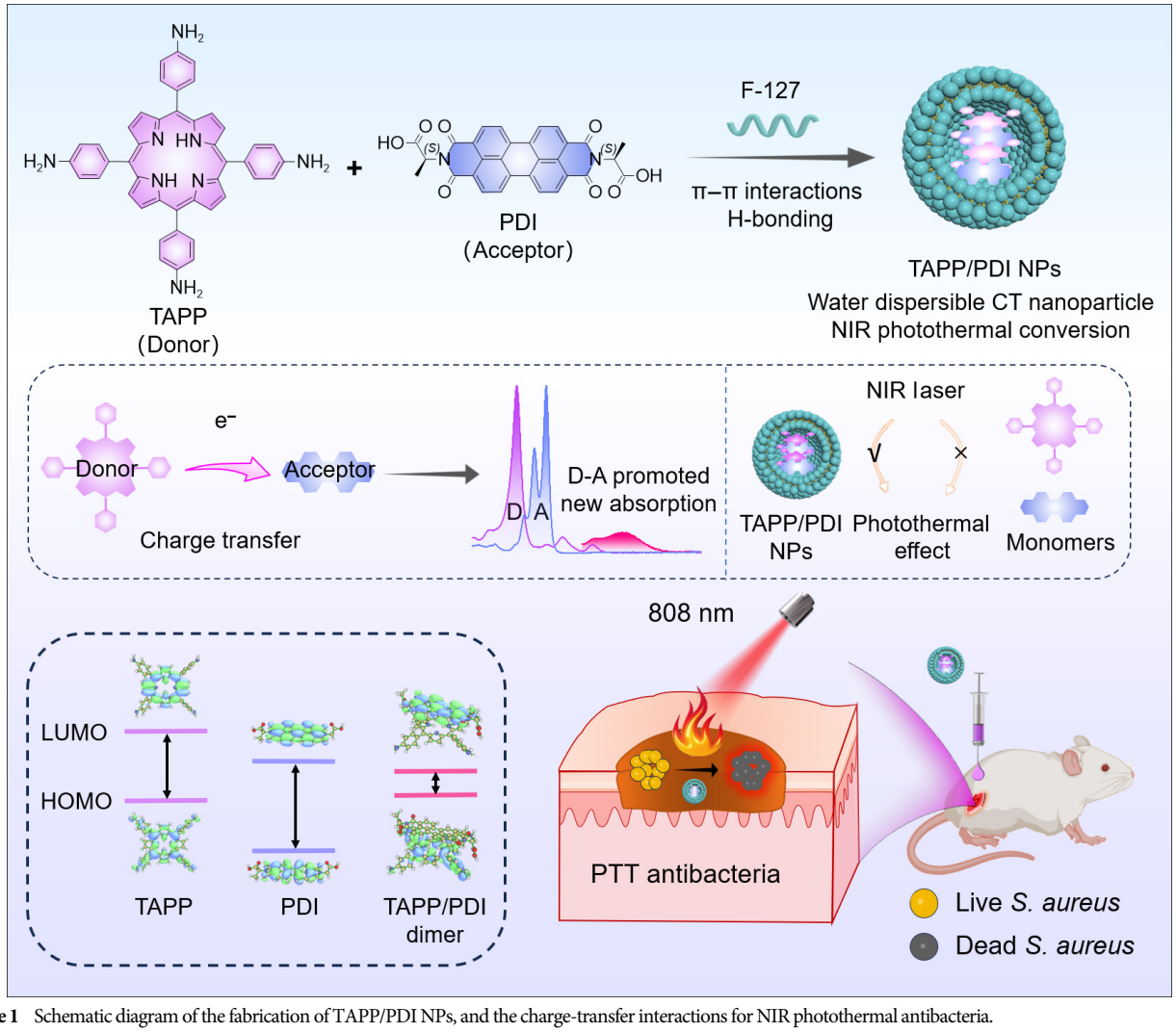

Scheme 1 Schematic diagram of the fabrication of TAPP/PDI NPs, and the charge-transfer interactions for NIR photothermal antibacteria.

feed ratio, finally decreased with 1:6 feed ratio. Due to the uniform morphology and intensified NIR peak, TAPP/PDI NPs fabricated at 1:2 feed ratio were used in the subsequent experiment. Moreover, the proportions of TAPP to PDI in the TAPP/PDI co-assemblies have been calculated according to the standard absorption curves. As shown in Table S1 in the ESM, the proportion of TAPP to PDI was calculated to be ~ 1:1 within TAPP/PDI NPs (1:2 feed ratio). This proportion was related to our subsequent theoretical calculation.

For comparison, TAPP nanoparticles and PDI nanowires (NWs) were obtained by using a similar method, as shown in Figs. 1(a)–1(d). TAPP self-assemblies showed non-uniform nanoparticular morphology with serious adhesions, and PDI self-assemblies displayed wirelike morphology. Different from TAPP NPs and PDI NWs, TAPP/PDI NPs showed relatively uniform nanoparticular morphology (Figs. 1(e) and 1(f)). The DLS of TAPP/PDI NPs was 99 nm with polydispersity index of 0.158 (Fig. 1(g)), indicating the uniform diameter, which was suitable for biological application. The DLS size of TAPP/PDI NPs (Fig. S5 in the ESM) did not show obvious change during 5 days, demonstrating their excellent dispersion. The UV–vis–NIR absorption spectra of TAPP NPs (Fig. 1(h)) showed B-band absorption peak at 455 nm and Q-band absorption peak at 587 and 678 nm with a red-shift of ~ 27.5 nm compared to that of the TAPP monomer (at 427.5 nm). The PDI nanowires showed absorption peak at 477 nm. While the absorption of TAPP/PDI showed significant red-shift to 758 nm, which should be attributed to the charge transfer from TAPP to PDI [20, 34, 35]. The fluorescence spectra of TAPP NPs displayed emission peak at 688 nm, and PDI nanowires demonstrated peaks at 544 and 590 nm (Fig. 1(i)). In contrast, TAPP/PDI NPs showed only weak peak at 544 and 588 nm from PDI, while the emission peaks from TAPP nearly disappear, further indicating the charge transfer from TAPP to PDI [34, 36]. Then the interactions between TAPP and PDI were investigated. We redissolved TAPP/PDI NPs in DMF, and found the obtained solution showed absorption peaks identical to TAPP free molecule and PDI free molecule (Fig. 1(j)), implying TAPP and PDI were co-assembled through the non-covalent interactions. FT-IR spectra of TAPP/PDI NPs displayed a broad peak at 3400 cm^{-1}, which belonged to the stretching vibration of the $-NH_2$ from TAPP and the –OH from PDI (Fig. 1(k)). Importantly, the TAPP powder showed N–H internal bending vibration peak at 1614 cm^{-1}, which shifted to 1599 cm^{-1} in TAPP/PDI NPs, indicating the hydrogen bonds existed in TAPP/PDI NPs derived from the interactions between the carboxylic acid group of PDI and the primary amine group of TAPP [37]. The XRD patterns of the TAPP/PDI NPs, TAPP NPs, and PDI NWs showed similar diffraction peak (Fig. S6 in the ESM), indicating the disordered nanostructures.

Inspired by the new NIR absorption, we then systematically studied the photoactivated properties of TAPP/PDI NPs illuminated by 808 nm laser. Firstly, the photothermal properties of TAPP/PDI co-assemblies with different feed ratios were

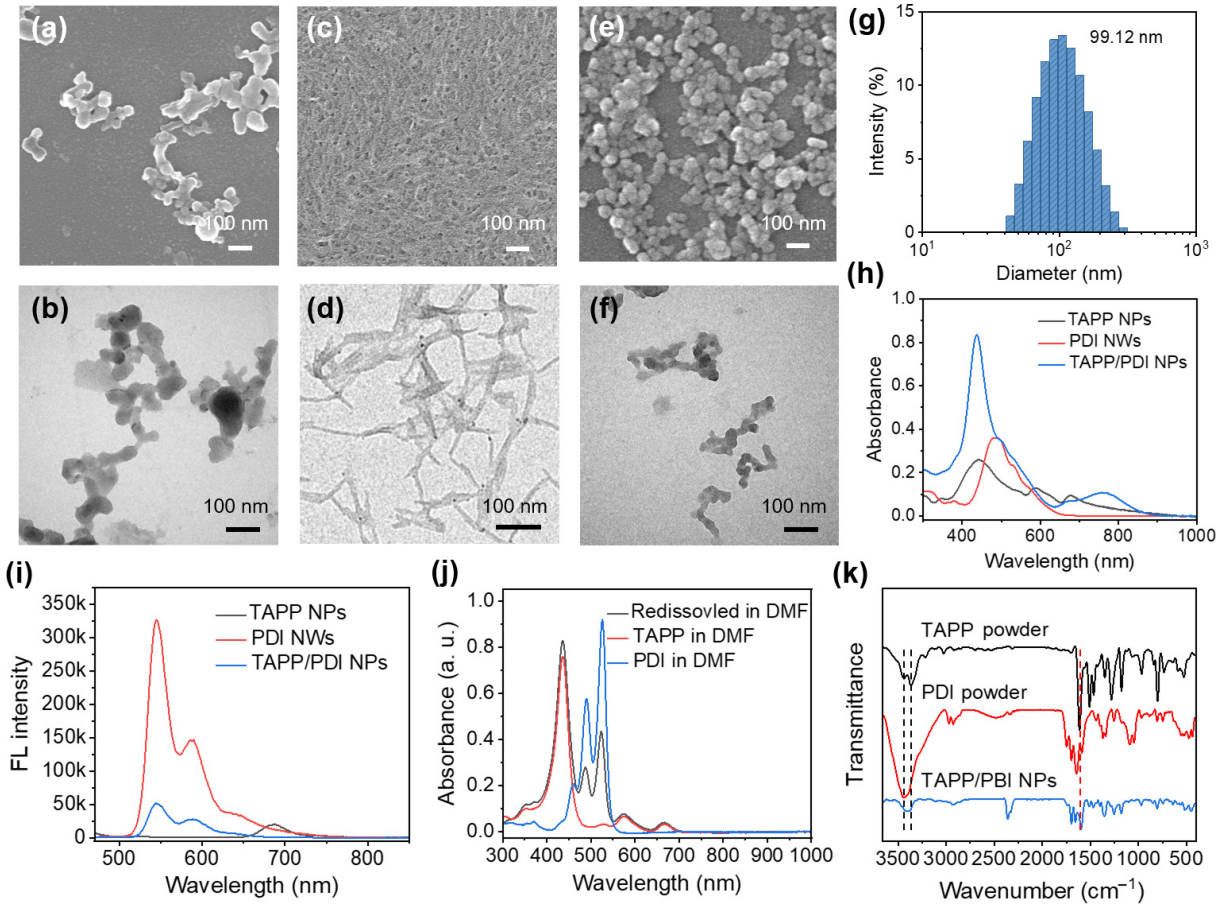

Figure 1 Morphology characterization and photophysical properties of the prepared samples. (a) SEM and (b) TEM images of TAPP NPs. (c) SEM and (d) TEM images of PDI NWs. (e) SEM image, (f) TEM image, and (g) DLS of TAPP/PDI NPs. (h) The absorption and (i) fluorescence spectra of TAPP NPs, PDI NWs, and TAPP/PDI NPs. (j) The absorption spectra recorded for TAPP/PDI NPs redissolved in DMF. (k) The FT-IR spectra of two monomer powder and TAPP/PDI NPs.

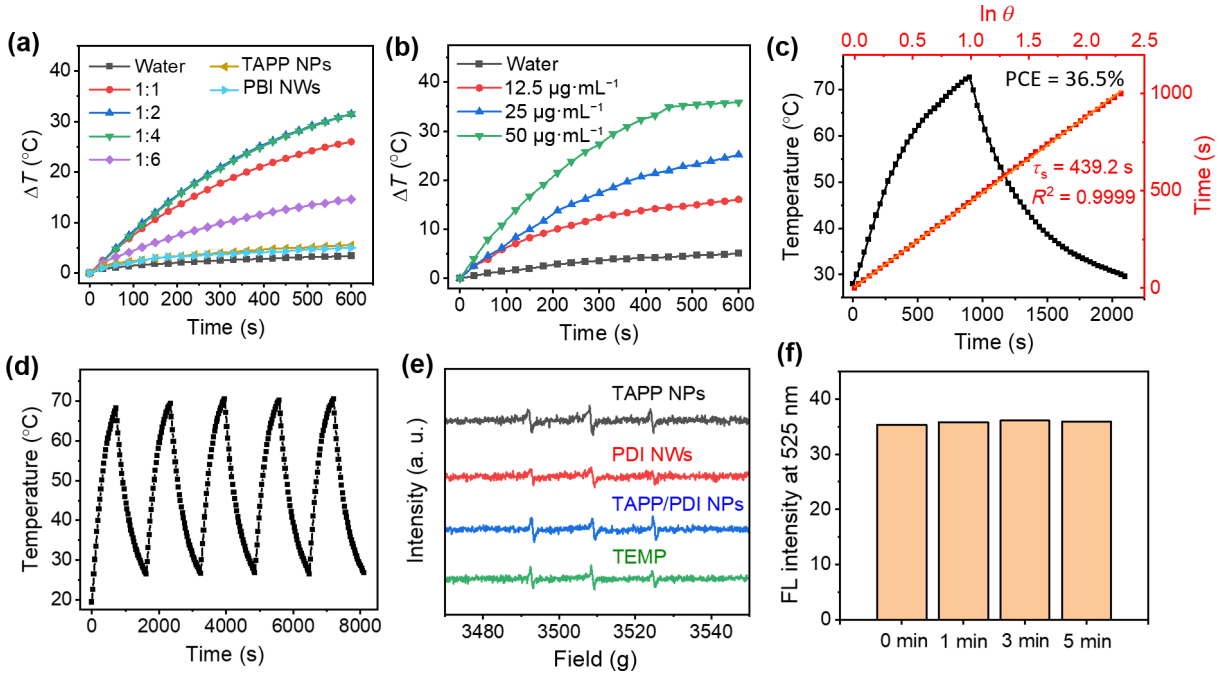

Figure 2 NIR light activated properties of the co-assemblies. (a) The temperature elevation of TAPP/PDI co-assemblies with different feed ratios, TAPP NPs (50 μg·mL^{-1}), and PDI NWs (50 μg·mL^{-1}). (b) The temperature elevation of TAPP/PDI NPs (feed ratio of 1:2) with different TAPP concentrations. (c) Heating and cooling curves of TAPP/PDI NPs under 808 nm laser irradiation (1.0 W·cm^{-2}) and corresponding cooling time constant (τ_s) calculation. (d) Photothermal stability of TAPP/PDI NPs for five irradiation cycles (808 nm, 1.0 W·cm^{-2}). (e) ESR results of singlet oxygen detection for TAPP NPs, PDI NWs, and TAPP/PDI NPs. (f) The fluorescence intensity (at 525 nm) of DCFH in TAPP/PDI NPs dispersion under laser illumination (808 nm, 1.0 W·cm^{-2}).

investigated (Fig. 2(a)). When the feed ratio of TAPP to PDI is 1:2 or 1:4, the TAPP/PDI co-assemblies showed temperature elevation (ΔT) of 31.5 °C, which was much higher than TAPP/PDI NPs with feed ratio of 1:1 (26 °C). When the feed ratio increased to 1:6, the obtained TAPP/PDI co-assembly showed weak temperature elevation (14.6 °C), in accordance with the weak NIR absorption. In comparison, TAPP NPs and PDI NWs showed the temperature elevation of 5.5 and 5.0 °C, which was only a little higher than the water, indicating TAPP NPs and PDI NWs are not suitable for NIR-excitable PTT. Then the temperature elevation of TAPP/PDI NPs at different concentrations (Fig. 2(b)) and different power densities (Fig. S7 in the ESM) were investigated. TAPP/PDI NPs showed the temperature elevation of 16.1, 25.2, and 35.9 °C at TAPP concentrations of 12.5, 25, and 50 μg·mL^{-1} irradiated by 808 nm laser (1.0 W·cm^{-2}). In addition, the temperature increased by 19.6, 27.5, and 35.9 °C at 0.5, 0.7, and 1.0 W·cm^{-2} (50 μg·mL^{-1}) with the laser power density rising. Thus, the photothermal properties of TAPP/PDI NPs varied with different concentrations and different laser densities. According to the Eqs. (1) and (2), the PCE of TAPP/PDI NPs was calculated to be 36.5% (Fig. 2(c)) [38, 39], surpassing that of commercial ICG (17.3%), Au nanorods (20.7%), CuSe nanocrystal (22%) and so forth [40–42]. TAPP/PDI NPs demonstrated no temperature decrease during five irradiation cycles (Fig. 2(d)), indicating their excellent photothermal stability.

To assess singlet oxygen ($^1O_2$) generation of TAPP/PDI NPs under NIR irradiation, we employed anthracene-9,10-dipropionic acid (ADPA) as a chemical capture agent, because the three absorbance peaks (359, 379, and 400 nm) of ADPA would decrease upon reacting with $^1O_2$ [9]. The absorbance of TAPP/PDI NPs, TAPP NPs, and PDI NWs remained virtually unchanged after 808 nm laser irradiation for 5 min (Fig. S8 in the ESM), indicating no $^1O_2$ production in any of these groups. The ESR spectra [43] further confirmed the absence of singlet oxygen generation (Fig. 2(e)). Furthermore, the ROS production performance of TAPP/PDI NPs was studied utilizing DCFH-DA probe [44]. Figure 2(f) showed that the DCFH fluorescence intensity in TAPP/PDI NPs dispersion remained the same under 808 nm laser irradiation, certifying no ROS generation by TAPP/PDI NPs.

We then investigated the intermolecular interactions between TAPP and PDI molecule through molecular dynamics simulation with Gromacs software (Fig. 3(a)) [45, 46] . After 1 ns of molecular dynamics simulation, the two closest molecules demonstrated the intermolecular center distance of 3.953 Å, which was characteristic of π–π conjugated stacking (Fig. 3(b)). Further analysis revealed that there also existed dynamic hydrogen bonds between the two monomers with the closest center distance (Fig. S9 and Video S1 in the ESM). Therefore, both π–π interactions and hydrogen bonds affect the stability and interaction characteristics of the molecules. Then the absorption spectra of the closest dimer as well as two monomers were simulated by adopting the B3LYP/6-31G** basis set. As demonstrated in Fig. 3(c), TAPP molecule showed the B-band and Q-band absorption peaks at 402 and 582 nm, respectively. PDI molecule displayed the B-band and Q-band absorption peaks at 341 and 524 nm, respectively. Compared with the two molecules, the dimer demonstrated the B-band absorption peak red-shifted to 406 nm, and the Q-band absorption peak significantly red-shifted to 664 nm. To further study the reasons for the spectral red-shift, detailed calculations were carried out on the absorption spectra. The calculation results are shown in Fig. 3(d) and Table S2 in the ESM. Table S2 in the ESM demonstrated that the dimer's B-band absorption was originated from the main orbital (45%) transition from the highest occupied molecular orbital (HOMO)-9 to the lowest unoccupied molecular orbital (LUMO)+3

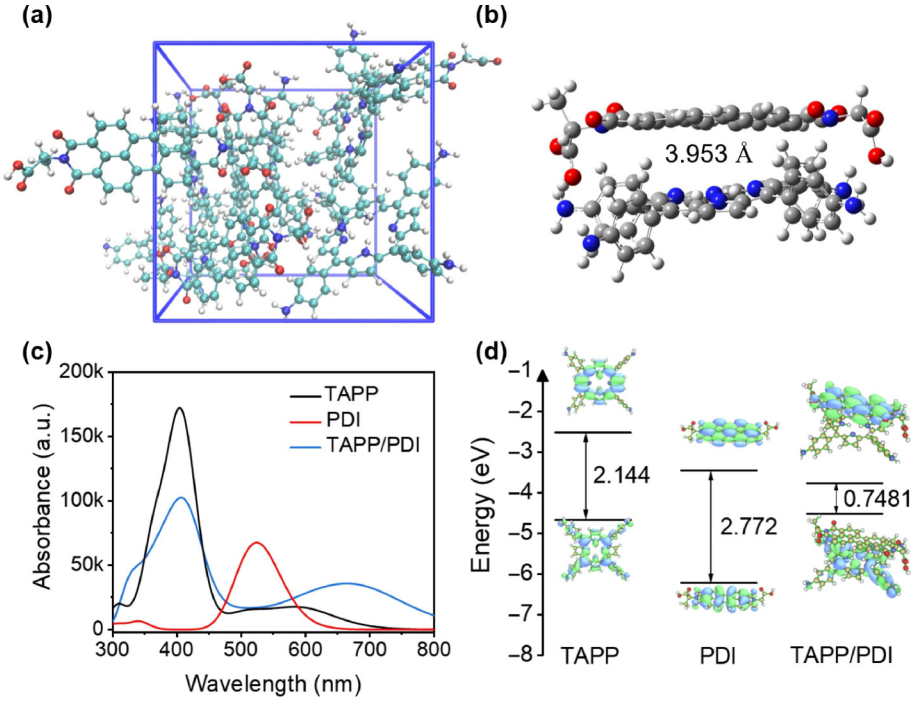

Figure 3 Theoretical calculations of intermolecular interactions, absorption spectra and energy gap. (a) The box of size 3 nm × 3 nm × 3 nm with 5 TAPP molecules and 5 PDI molecules in it. (b) The picture of TAPP/PDI dimer with the closest intermolecular distance. (c) The calculated absorption spectra and (d) the HOMO/LUMO energy gap of TAPP, PDI, and the closest TAPP/PDI dimer.

orbital (Fig. S10 in the ESM); the dimer's Q-band absorption was derived from the main orbital (48%) transition from the HOMO-1 to the LUMO+2 orbital; the number of transition orbital in the dimer increased compared with that of two monomers, resulting in the broadened dimer's B-band and Q-band absorption. Besides, the oscillator strength of the dimer's B-band (f_B) and Q-band (f_Q) decreased compared with that of two monomers. As shown in Fig. 3(d), the energy gaps of the two monomers were 2.144 and 2.772 eV, while the energy gap of the dimer significantly decreased to 0.7481 eV, thus TAPP/PDI NPs show obvious spectral redshift. Moreover, the spin-orbit coupling (SOC) constants of the dimer and two monomers was obtained through TD-DFT calculations. The SOC value of the dimer is calculated to be 0.21552 (Table 1), which was too low and could not result in an adequate intersystem crossing (ISC) efficiency. Therefore, the energy dissipation process mainly occurs through internal conversion.

Given the photothermal properties of TAPP/PDI NPs, their antimicrobial potential was systematically investigated against Gram-positive *S. aureus* and Gram-negative *E. coli* pathogens. Quantitative assessment of bactericidal efficacy was performed via standardized colony-forming unit (CFU) enumeration assays. As shown in Figs. 4(a)–4(c), TAPP/PDI NPs (100 μg·mL^{-1}) do not demonstrate antibacterial effect under dark condition, while TAPP/PDI NPs irradiation could eradicate *S. aureus* or *E. coli* effectively under 808 nm laser illumination, proving the well antibacterial ability of TAPP/PDI NPs. Then, bacterial membrane integrity and morphological changes induced by the treatments were visualized via SEM. As displayed in Fig. 4(d), the cellular membranes of both *S. aureus* and *E. coli* remain structurally intact

Table 1 The SOC constants of the monomers and TAPP/PDI dimer

	TAPP	PDI	TAPP/PDI
SOC (cm^{-1})	1.37515	0.01364	0.21552

in the control (saline), NIR, and TAPP/PDI NPs groups. In contrast, significant morphological disruptions, including membrane collapse and the intracellular contents leakage, were observed in bacterial cells of TAPP/PDI NPs plus laser group. These findings further corroborated the potent antibacterial activity of TAPP/PDI NPs under photothermal stimulation. Bacterial viability was also visually analyzed via SYTO9/propidium iodide (PI) dual staining, providing additional validation of the photothermal antibacterial effects of the nanoparticles (Fig. 4(e)). For control, NIR, and TAPP/PDI NPs groups, green fluorescence (live bacteria) dominated absolutely. However, for TAPP/PDI NPs combined laser group, red fluorescence (dead bacteria) dominated thoroughly. The photothermal antibacterial performance of TAPP/PDI NPs was also compared with several NIR PTAs (Table S3 in the ESM), which showed the considerable antibacterial effect of TAPP/PDI NPs.

Before evaluating the *in vivo* antibacterial performance of TAPP/PDI NPs, their hemocompatibility and cytotoxicity were assessed. Figure S11 in the ESM shows the hemolysis ratio of the TAPP/PDI NPs dispersions with different concentrations. The hemolysis ratios of TAPP/PDI NPs groups were less than 5%, and erythrocyte morphology remained unaltered even the concentration increased to 400 μg·mL^{-1}. The cytotoxicity of TAPP/PDI NPs was detected in HeLa cell lines (Fig. S12 in the ESM). CCK-8 assays [47] showed no significant reduction in cell viability after 24 h incubation with varying concentrations of TAPP/PDI NPs (0 to 400 μg·mL^{-1}). The therapeutic process can be illustrated in Fig. 5(a). We randomly divided the *S. aureus*-infected mice into 4 groups: Control, NIR, TAPP/PDI NPs, and TAPP/PDI NPs + NIR. As exhibited in Figs. 5(b) and 5(c), the temperature of infected wound area of the mice in TAPP/PDI NPs + Laser group could reach 60.2 °C within 10 min. In contrast, the temperature change of the NIR group was not evident. This result identified that

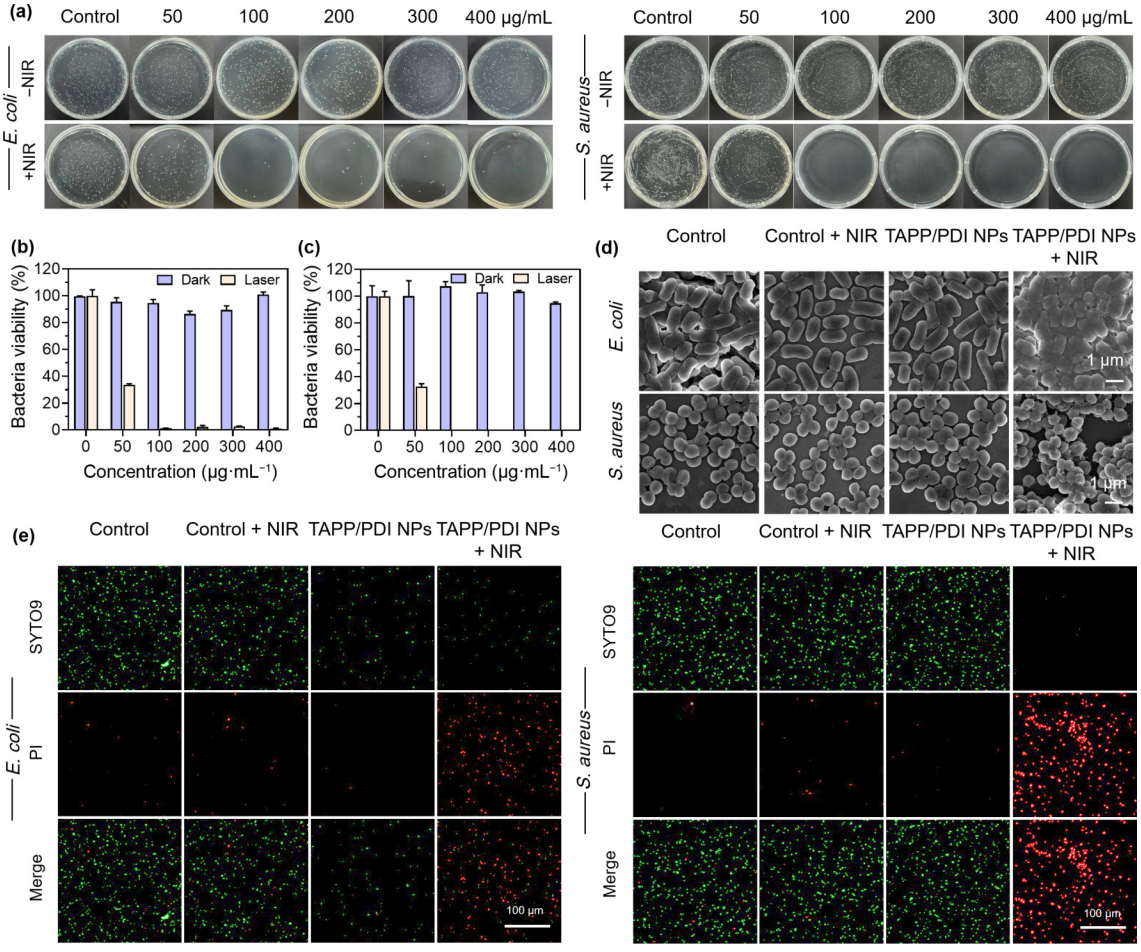

Figure 4 *In vitro* antibacterial investigation. (a) Agar plate images and ((b) and (c)) corresponding colonies statistical data after *E. coli* or *S. aureus* incubated with TAPP/PDI NPs at varying concentration with and without 808 nm laser illumination (1.0 W·cm^{-2}, 10 min). (d) SEM images and (e) SYTO9/PI staining results of *E. coli* or *S. aureus* after different treatments (300 μg·mL^{-1} of TAPP/PDI NPs).

TAPP/PDI NPs could serve as an advanced photothermal dressing for accelerating wound healing. To assess the therapeutic efficacy, infected wound sites were photographed after different treatments. As demonstrated in Fig. 5(d), the TAPP/PDI NPs + NIR group demonstrated superior wound healing efficacy compared to other groups. To evaluate bacterial load in the infected wounds, standard bacterial culture assays were performed. Results revealed significant reduction in bacterial counts in the TAPP/PDI NPs + NIR group relative to the other three groups (Fig. 5(e)), which could be attributed to the potent photothermal activity of TAPP/PDI NPs. Furthermore, histological analysis of infected wound tissues was conducted via H&E and Masson staining on day 10. There were incomplete epidermis and substantial inflammatory cell infiltration in the infected wounds in the groups of control, NIR and TAPP/PDI NPs, while the tissues treated with TAPP/PDI NPs plus laser displayed evident epithelialization and collagen fiber formation (blue stained area) (Fig. 5(g)) [48, 49]. The experimental data demonstrate that TAPP/PDI NPs with laser irradiation could facilitate wound healing and possess potent antibacterial efficacy *in vivo*.

To ensure the biological application of TAPP/PDI NPs, a comprehensive biosafety assessment is necessary. During the 10-day treatments, the mice body weight in all groups gradually increased (Fig. 5(f)), indicating minimal systemic toxicity at the used dosage. On day 10 post-treatments, the major organs were obtained for histopathological examination via H&E staining. As shown in Fig. S13 in the ESM, the mice in the TAPP/PDI NPs + NIR group show no observable histopathological abnormalities compared to the control group. To further assess the biosafety *in vivo*, blood routine test and blood biochemistry analyses were conducted from TAPP/PDI NPs + NIR group, with healthy mice and control group as comparison. No significant differences were noticed in hematological and biochemical parameters among the three groups (Fig. S14 in the ESM), further confirming the favorable biosafety profile of TAPP/PDI NPs.

4 Conclusions

In conclusion, CTA TAPP/PDI NPs with NIR absorption have been successfully fabricated through the supramolecular assembly of TAPP and PDI mediated by the π–π interactions and hydrogen bonding interactions. TAPP/PDI NPs exhibit profitable absorption in the NIR region and fluorescence quenching, due to the charge transfer from TAPP to PDI. Furthermore, TAPP/PDI NPs possess satisfactory photothermal property under 808 nm laser illumination. According to molecular dynamic simulation, the co-assembly forces were confirmed to originate from π–π interactions and hydrogen bond interactions. Moreover, the energy gap of TAPP/PDI dimer was significantly narrowed, accompanied by small SOC, which in favor of the NIR light activated internal

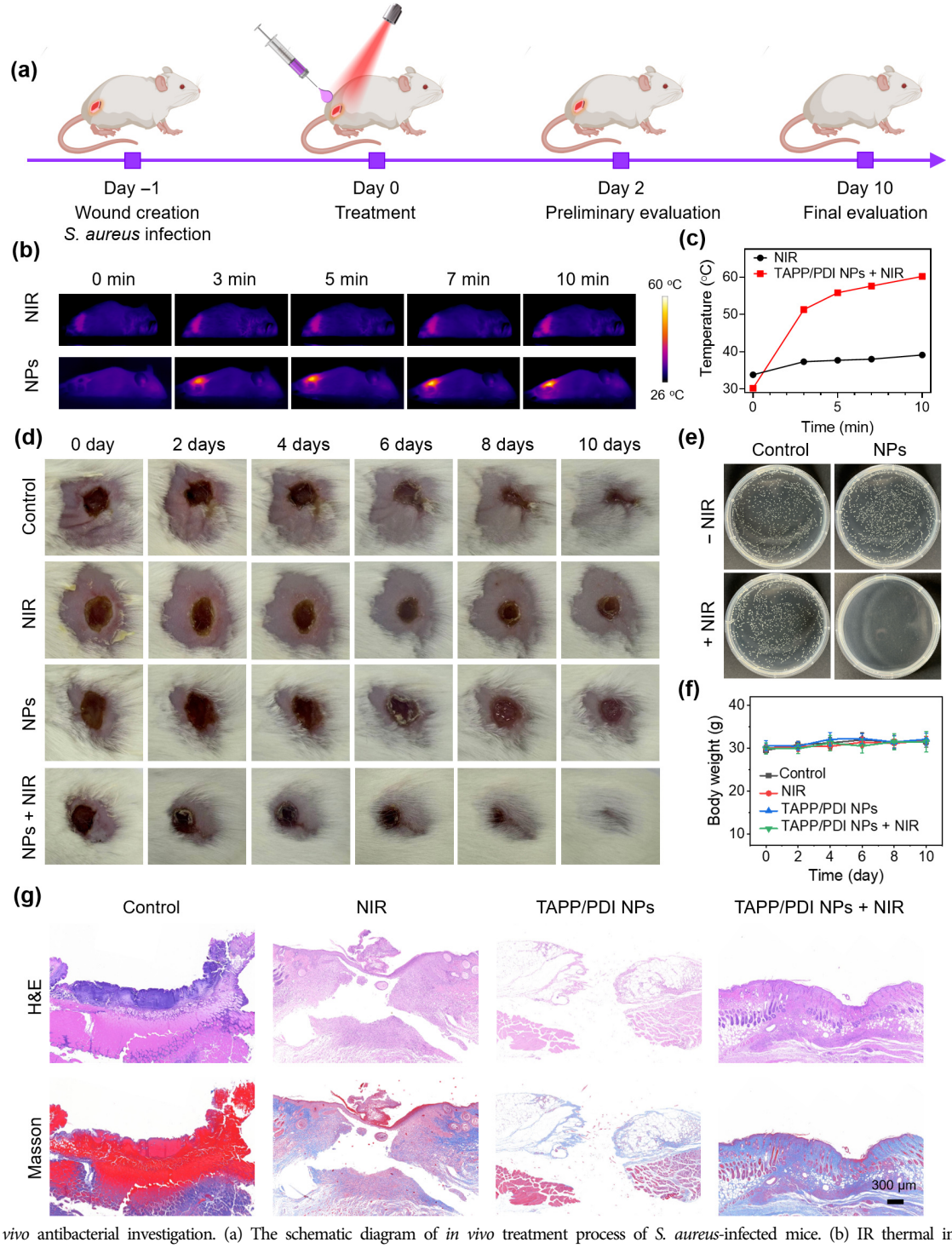

Figure 5 *In vivo* antibacterial investigation. (a) The schematic diagram of *in vivo* treatment process of *S. aureus*-infected mice. (b) IR thermal images and (c) corresponding tumor temperature changes of mice upon 808 nm laser irradiation (1.0 W·cm^{-2}, 10 min). (d) Representative wound images upon different treatments. (e) LB spread a plate of *S. aureus*-infected wounds on day 10. (f) Body weight changes of mice. (g) H&E and Masson staining infected tissues on day 10.

conversion of TAPP/PDI NPs. As evidenced by both *in vitro* and *in vivo* experimental results, TAPP/PDI NPs could efficiently kill bacteria under 808 nm laser irradiation. This supramolecular approach provides a robust platform for designing nanoparticle systems with tailored NIR absorption properties for photothermal therapy.

Electronic Supplementary Material: Supplementary material (SEM images and absorption spectra of TAPP/PDI co-assemblies, the proportions of TAPP to PDI in the co-assemblies, photothermal elevation curves, the variation of the number of hydrogen bond over time (figure and video), the molecular orbitals of TAPP/PDI dimer, comparison of photothermal antibacterial performance, hemolysis analysis, CCK-8 assay, H&E staining tissue section, and routine blood test and blood biochemistry data) is available in the online version of this article at https://doi.org/10.26599/NR.2025.94907835.

Data availability

All data needed to support the conclusions in the paper are presented in the manuscript and the Electronic Supplementary Material. Additional data related to this paper may be requested from the corresponding author upon request.

Acknowledgements

This work is granted by the National Natural Science Foundation of China (Nos. 52102345 and U21A2085), the Zhongyuan High Level Talents Special Support Plan (No. 204200510009), China Postdoctoral Science Foundation (No. 2024M750766), and the Scientific and Technological Innovation Team in University of Henan Province (No. 20IRTSTHN001).

Declaration of competing interest

All the contributing authors report no conflict of interests in this work.

Author contribution statement

Y. S. L.: Characterization, validation, antibacterial experiments, writing and revising manuscript. Y. Y. S.: Synthesis, characterization, antibacterial experiments, data curation. L. M. Y.: Theoretical calculations. J. L. Q and C. H.: Antibacterial experiments *in vivo*. J. Y. W.: Revising manuscript, funding acquisition. Y. Z.: SEM characterization, data analyzing. X. Y. Y.: Data curation, project administration, funding acquisition, writing and revising manuscript. F. B.: Experimental design, project administration, funding acquisition, writing and revising manuscript. All the authors have approved the final manuscript.

Informed consent

Not applicable.

Ethics statement

The animal experiments were approved by the Medical and Scientific Research Ethics Committee of the Henan University School of Medicine (Ethical code: HUSOM2025-707).

Use of AI statement

None.

References

[1] Liang, S.; Liu, Y. F.; Zhu, H. Q.; Liao, G. F.; Zhu, W. Z.; Zhang, L. Emerging nitric oxide gas-assisted cancer photothermal treatment. *Exploration* **2024**, *4*, 20230163.

[2] Chen, J.; Chen, T. X.; Fang, Q. L.; Pan, C. S.; Akakuru, O. U.; Ren, W. Z.; Lin, J.; Sheng, A. Z.; Ma, X. H.; Wu, A. G. Gd_2O_3/b–TiO_2 composite nanoprobes with ultra-high photoconversion efficiency for MR image-guided NIR-II photothermal therapy. *Exploration* **2022**, *2*, 20220014.

[3] Song, S.; Yang, N.; He, D.; Li, Y.; Akhtar, M. H.; Liu, C.; Li, X. W.; Shen, X. D.; Yu, C. Cyanine-based nanoparticles for near-infrared triggered photothermal therapy against *S. aureus*. *New J. Chem.* **2024**, *48*, 5674–5680.

[4] Fu, H.; Zhang, Y. X.; Wang, C.; Sun, Z. C.; Lv, S. Y.; Xiao, M. H.; Wu, K. Y.; Shi, L. Q.; Zhu, C. L. A universal strategy to enhance photothermal conversion efficiency by regulating the molecular aggregation states for safe photothermal therapy of bacterial infections. *Biomater. Sci.* **2024**, *12*, 2914–2929.

[5] Geng, Z. M.; Cao, Z. P.; Liu, J. Y. Recent advances in targeted antibacterial therapy basing on nanomaterials. *Exploration* **2023**, *3*, 20210117.

[6] Cao, R. H.; Wang, G. Y.; Ren, X. T.; Duan, P. C.; Wang, L.; Li, Y. S.; Chen, X.; Zhu, R.; Jia, Y.; Bai, F. Self-assembled porphyrin nanoleaves with unique crossed transportation of photogenerated carriers to enhance photocatalytic hydrogen production. *Nano Lett.* **2022**, *22*, 157–163.

[7] Cao, R. H.; Wang, J. H.; Li, Y. S.; Sun, J. J.; Bai, F. Morphology-controlled porphyrin nanocrystals with enhanced photocatalytic hydrogen production. *Nano Res.* **2022**, *15*, 5719–5725.

[8] Wang, M. Y.; Huang, G.; You, Z. Q.; Jia, R. X.; Zhong, Y.; Bai, F. Progress of porphyrin-based nanoassemblies for cancer theranostics. *Chem. Res. Chin. Univ.* **2023**, *39*, 612–623.

[9] Yang, L. F.; Liu, Y. Q.; Ren, X. R.; Jia, R. X.; Si, L. L.; Bao, J. S.; Shi, Y. Y.; Sun, J. J.; Zhong, Y.; Duan, P. C. et al. Microemulsion-assisted self-assembly of indium porphyrin photosensitizers with enhanced photodynamic therapy. *ACS Nano* **2024**, *18*, 3161–3172.

[10] Liu, Y. Q.; Wang, L.; Feng, H. X.; Ren, X. T.; Ji, J. J.; Bai, F.; Fan, H. Y. Microemulsion-assisted self-assembly and synthesis of size-controlled porphyrin nanocrystals with enhanced photocatalytic hydrogen evolution. *Nano Lett.* **2019**, *19*, 2614–2619.

[11] Wang, X.; Wang, J. F.; Wang, J. H.; Zhong, Y.; Han, L. L.; Yan, J. L.; Duan, P. C.; Shi, B. Y.; Bai, F. Noncovalent self-assembled smart gold(III) porphyrin nanodrug for synergistic chemo-photothermal therapy. *Nano Lett.* **2021**, *21*, 3418–3425.

[12] Wang, J. F.; Zhong, Y.; Wang, X.; Yang, W. T.; Bai, F.; Zhang, B. B.; Alarid, L.; Bian, K. F.; Fan, H. Y. pH-dependent assembly of porphyrin-silica nanocomposites and their application in targeted photodynamic therapy. *Nano Lett.* **2017**, *17*, 6916–6921.

[13] Zhao, H.; Wang, Y.; Chen, Q.; Liu, Y.; Gao, Y. J.; Müllen, K.; Li, S. L.; Narita, A. A nanographene-porphyrin hybrid for near-infrared-II phototheranostics. *Adv. Sci.* **2024**, *11*, 2309131.

[14] Cao, Y. B.; Wei, D.; Yang, L. X.; Luo, Z. J.; Yu, P. W.; Li, H.; Zhang, C.; Liu, X. L.; Wu, F. S.; Wu, M. et al. Nanoplatform self-assembly from small molecules of porphyrin derivatives for NIR-II fluorescence imaging guided photothermal-immunotherapy. *Adv. Healthcare Mater.* **2022**, *11*, 2102526.

[15] Bodedla, G. B.; Piradi, V.; Imran, M.; Zhao, J. Z.; Zhu, X. J.; Wong, W. Y. Visible-to-near-infrared light-harvesting A-π-D-π-A porphyrins for boosted photocatalytic hydrogen evolution. *J. Mater. Chem. A* **2023**, *11*, 1473–1481.

[16] Tian, S.; Bai, H. T.; Li, S. L.; Xiao, Y. F.; Cui, X.; Li, X. Z.; Tan, J. H.; Huang, Z. M.; Shen, D.; Liu, W. M. et al. Water-soluble organic nanoparticles with programable intermolecular charge transfer for NIR-II photothermal anti-bacterial therapy. *Angew. Chem., Int. Ed.* **2021**, *60*, 11758–11762.

[17] Ou, C. J.; Na, W.; Ge, W.; Huang, H.; Gao, F.; Zhong, L. P.; Zhao, Y. X.; Dong, X. C. Biodegradable charge-transfer complexes for glutathione depletion induced ferroptosis and NIR-II photoacoustic imaging guided cancer photothermal therapy. *Angew. Chem., Int. Ed.* **2021**, *60*, 8157–8163.

[18] Wu, Q. H.; Xia, R.; Li, C. N.; Li, Y. T.; Sun, T. T.; Xie, Z. G.; Jing, X. B. Nanoscale aggregates of porphyrins: Red-shifted absorption, enhanced absorbance and phototherapeutic activity. *Mater. Chem. Front.* **2021**, *5*, 8333–8340.

[19] Li, P.; Xu, G. J.; Wang, N. N.; Guan, B.; Zhu, S. Q.; Chen, P. L.; Liu, M. H. 0D, 1D, and 2D supramolecular nanoassemblies of a porphyrin: Controllable assembly, and dimensionality-dependent catalytic performances. *Adv. Funct. Mater.* **2021**, *31*, 2100367.

[20] Wu, Q. H.; Xia, R.; Wen, H.; Sun, T. T.; Xie, Z. G. Nanoscale

porphyrin assemblies based on charge-transfer strategy with enhanced red-shifted absorption. *J. Colloid Interface Sci.* **2022**, *627*, 554–561.
[21] Li, C. W.; Gao, Y.; Huang, R.; Fang, L.; Sun, Y. Y.; Yang, Y. L.; Gou, S. H.; Zhao, J. An effective supramolecular approach to boost the photodynamic therapy efficacy of a near-infrared activating perylene diimide-based photosensitizer. *ACS Mater. Lett.* **2022**, *4*, 657–664.
[22] Li, Y. J.; Jiang, M. L.; Yan, M. M.; Ye, J. T.; Li, Y.; Dehaen, W.; Yin, S. C. Near-infrared boron-dipyrrin (BODIPY) nanomaterials: Molecular design and anti-tumor therapeutics. *Coord. Chem. Rev.* **2024**, *506*, 215718.
[23] Zhao, J.; Huang, R.; Gao, Y.; Xu, J. D.; Sun, Y. Y.; Bao, J. Y.; Fang, L.; Gou, S. H. Realizing near-infrared (NIR)-triggered type-I PDT and PTT by maximizing the electronic exchange energy of perylene diimide-based photosensitizers. *ACS Mater. Lett.* **2023**, *5*, 1752–1759.
[24] Yang, J.; Jing, J. F.; Li, W. L.; Zhu, Y. F. Electron donor-acceptor interface of TPPS/PDI boosting charge transfer for efficient photocatalytic hydrogen evolution. *Adv. Sci.* **2022**, *9*, 2201134.
[25] Zhu, L.; Zhang, M.; Zhong, W. K.; Leng, S. F.; Zhou, G. Q.; Zou, Y. C.; Su, X.; Ding, H.; Gu, P. Y.; Liu, F. et al. Progress and prospects of the morphology of non-fullerene acceptor based high-efficiency organic solar cells. *Energy Environ. Sci.* **2021**, *14*, 4341–4357.
[26] Wang, J. F.; Wang, Z. J.; Zhong, Y.; Zou, Y.; Wang, C.; Wu, H. G.; Lee, A.; Yang, W. T.; Wang, X.; Liu, Y. J. et al. Central metal-derived co-assembly of biomimetic GdTPP/ZnTPP porphyrin nanocomposites for enhanced dual-modal imaging-guided photodynamic therapy. *Biomaterials* **2020**, *229*, 119576.
[27] Bao, J. S.; Wang, J. F.; Chen, S. D.; Liu, S. Q.; Wang, Z.; Zhang, W. W.; Zhao, C. H.; Sha, Y. L.; Yang, X. Y.; Li, Y. S. et al. Coordination self-assembled AuTPyP-Cu metal-organic framework nanosheets with pH/ultrasound dual-responsiveness for synergistically triggering cuproptosis-augmented chemotherapy. *ACS Nano* **2024**, *18*, 9100–9113.
[28] Tian, T.; Bao, J. S.; Wang, J. H.; Wang, J. F.; Ge, Y.; Li, Z. Y.; Gao, S. Q.; You, Z. Q.; Yang, X. Y.; Zhong, Y. et al. Co-assembly of FeTPP@Fe_3O_4 nanoparticles with photo-enhanced catalytic activity for synergistic tumor therapy. *Nano Res.* **2022**, *15*, 9114–9124.
[29] Wang, J. F.; Shangguan, P.; Lin, M.; Fu, L. B.; Liu, Y. S.; Han, L. L.; Chen, S. D.; Wang, X.; Lu, M. Y.; Luo, Z. Q. et al. Dual-site förster resonance energy transfer route of upconversion nanoparticles-based brain-targeted nanotheranostic boosts the near-infrared phototherapy of glioma. *ACS Nano* **2023**, *17*, 16840–16853.
[30] Wu, Q. H.; Liu, J. W.; Wang, H. Y.; Wen, H.; Sun, T. T.; Xie, Z. G. Carrier-free porphyrin-based supramolecular complexes for near-infrared photothermal-enhanced wound healing. *Chem. Eng. J.* **2024**, *502*, 158128.
[31] Lu, T.; Chen, F. W. Multiwfn: A multifunctional wavefunction analyzer. *J. Comput. Chem.* **2012**, *33*, 580–592.
[32] Lu, T. A comprehensive electron wavefunction analysis toolbox for chemists, Multiwfn. *J. Chem. Phys.* **2024**, *161*, 082503.
[33] Humphrey, W.; Dalke, A.; Schulten, K. VMD: Visual molecular dynamics. *J. Mol. Graph.* **1996**, *14*, 33–38.
[34] Wang, B. Z.; Zheng, S. S.; Saha, A.; Bao, L. P.; Lu, X.; Guldi, D. M. Understanding charge-transfer characteristics in crystalline nanosheets of fullerene/(metallo)porphyrin cocrystals. *J. Am. Chem. Soc.* **2017**, *139*, 10578–10584.
[35] Wang, Y.; Wu, H.; Zhu, W. G.; Zhang, X. T.; Liu, Z. Y.; Wu, Y. S.; Feng, C. F.; Dang, Y. F.; Dong, H. L.; Fu, H. B. et al. Cocrystal engineering: Toward solution-processed near-infrared 2D organic cocrystals for broadband photodetection. *Angew. Chem., Int. Ed.* **2021**, *60*, 6344–6350.
[36] Zieleniewska, A.; Lodermeyer, F.; Roth, A.; Guldi, D. M. Fullerenes-how 25 years of charge transfer chemistry have shaped our understanding of (interfacial) interactions. *Chem. Soc. Rev.* **2018**, *47*, 702–714.
[37] Wang, Y. J.; Zhang, X. N.; Song, Y. H.; Zhao, Y. P.; Chen, L.; Su, F. M.; Li, L. B.; Wu, Z. L.; Zheng, Q. Ultrastiff and tough supramolecular hydrogels with a dense and robust hydrogen bond network. *Chem. Mater.* **2019**, *31*, 1430–1440.
[38] Liu, G. Y.; Zhu, J. W.; Guo, H.; Sun, A. H.; Chen, P.; Xi, L.; Huang, W.; Song, X. J.; Dong, X. C. Mo_2C-derived polyoxometalate for NIR-II photoacoustic imaging-guided chemodynamic/photothermal synergistic therapy. *Angew. Chem., Int. Ed.* **2019**, *58*, 18641–18646.
[39] Jia, J.; Liu, G. Y.; Xu, W. J.; Tian, X. L.; Li, S. B.; Han, F.; Feng, Y. H.; Dong, X. C.; Chen, H. Y. Fine-tuning the homometallic interface of Au-on-Au nanorods and their photothermal therapy in the NIR-II window. *Angew. Chem., Int. Ed.* **2020**, *59*, 14443–14448.
[40] Zheng, M. B.; Zhao, P. F.; Luo, Z. Y.; Gong, P.; Zheng, C. F.; Zhang, P. F.; Yue, C. X.; Gao, D. Y.; Ma, Y. F.; Cai, L. T. Robust ICG theranostic nanoparticles for folate targeted cancer imaging and highly effective photothermal therapy. *ACS Appl. Mater. Interfaces* **2014**, *6*, 6709–6716.
[41] Wang, B. K.; Wang, J. H.; Liu, Q.; Huang, H.; Chen, M.; Li, K. Y.; Li, C. Z.; Yu, X. F.; Chu, P. K. Rose-bengal-conjugated gold nanorods for *in vivo* photodynamic and photothermal oral cancer therapies. *Biomaterials* **2014**, *35*, 1954–1966.
[42] Hessel, C. M.; Pattani, V. P.; Rasch, M.; Panthani, M. G.; Koo, B.; Tunnell, J. W.; Korgel, B. A. Copper selenide nanocrystals for photothermal therapy. *Nano Lett.* **2011**, *11*, 2560–2566.
[43] Wang, W. T.; Wu, F.; Zhang, Q. C.; Zhou, N. L.; Zhang, M.; Zheng, T.; Li, Y. Y.; Tang, B. Z. Aggregation-induced emission nanoparticles for single near-infrared light-triggered photodynamic and photothermal antibacterial therapy. *ACS Nano* **2022**, *16*, 7961–7970.
[44] Xu, P. J.; Wen, C. C.; Gao, C. J.; Liu, H. H.; Li, Y. S.; Guo, X. L.; Shen, X. C.; Liang, H. Near-infrared-II-activatable self-assembled manganese porphyrin-gold heterostructures for photoacoustic imaging-guided sonodynamic-augmented photothermal/photodynamic therapy. *ACS Nano* **2024**, *18*, 713–727.
[45] Abraham, M. J.; Murtola, T.; Schulz, R.; Páll, S.; Smith, J. C.; Hess, B.; Lindahl, E. GROMACS: High performance molecular simulations through multi-level parallelism from laptops to supercomputers. *SoftwareX* **2015**, *1–2*, 19–25.
[46] Páll, S.; Abraham, M. J.; Kutzner, C.; Hess, B.; Lindahl, E. Tackling exascale software challenges in molecular dynamics simulations with GROMACS. *Solving Software Challenges for Exascale* **2015**, *8759*, 3–27.
[47] Li, X. X.; Wang, W.; Gao, Q. X.; Lai, S. S.; Liu, Y.; Zhou, S. T.; Yan, Y.; Zhang, J.; Wang, H. H.; Wang, J. M. et al. Intelligent bacteria-targeting ZIF-8 composite for fluorescence imaging-guided photodynamic therapy of drug-resistant superbug infections and burn wound healing. *Exploration* **2024**, *4*, 20230113.
[48] Lv, X. Y.; Jiang, J. G.; Ren, J.; Li, H.; Yang, D. L.; Song, X. J.; Hu, Y. L.; Wang, W. J.; Dong, X. C. Nitric oxide-assisted photodynamic therapy for enhanced penetration and hypoxic bacterial biofilm elimination. *Adv. Healthcare Mater.* **2023**, *12*, 2302031.
[49] Li, H.; Jiang, J. G.; Lv, X. Y.; Xu, Y.; Wang, W. J.; Yang, D. L.; Dong, X. C. Enzyme-like photocatalytic octahedral Rh/Ag_2MoO_4 accelerates diabetic wound healing by photo-eradication of pathogen and relieving wound hypoxia. *Small* **2024**, *20*, 2402723.